

On the nature of inhomogeneous weak localization of charge carriers in the heavy fermion compound CeB_6

A N Azarevich, A V Bogach, O N Khrykina, N B Bolotina, V M Gridchina, S Yu Gavrilkin, A Yu Tsvetkov, V V Voronov, K Flachbart, S Gabani, and N E Sluchanko

Citation: Chin. Phys. B, 2026, 35 (**3**): 037202. DOI: 10.1088/1674-1056/adfbdd
http://cpb.iphy.ac.cn; http://iopscience.iop.org/cpb

What follows is a list of articles you may be interested in

Regulating Anderson localization with structural defect disorder

Mouyang Cheng(程谋阳), Haoxiang Chen(陈浩翔), and Ji Chen(陈基)
Chin. Phys. B, 2024, 33 (**10**): 107201. DOI: 10.1088/1674-1056/ad711c

Current-perpendicular-to-plane transport properties of 2D ferromagnetic material $CrTe_2$

Jin Wang(王瑾), Yu Liu(刘宇), Taikun Wang(王太坤), Yongkang Xu(徐永康), Shuanghai Wang(王双海), Kun He(何坤), Yafeng Deng(邓亚峰), Pengfei Yan(闫鹏飞), and Liang He(何亮)
Chin. Phys. B, 2024, 33 (**9**): 097201. DOI: 10.1088/1674-1056/ad5af1

Higher-order topological Anderson insulator on the Sierpiński lattice

Huan Chen(陈焕), Zheng-Rong Liu(刘峥嵘), Rui Chen(陈锐), and Bin Zhou(周斌)
Chin. Phys. B, 2024, 33 (**1**): 017202. DOI: 10.1088/1674-1056/ad09d4

Weak antilocalization and interaction-induced localization of Dirac and Weyl Fermions in topological insulators and semimetals

Hai-Zhou Lu(卢海舟), Shun-Qing Shen(沈顺清)
Chin. Phys. B, 2016, 25 (**11**): 117202. DOI: 10.1088/1674-1056/25/11/117202

Localization correction to the anomalous Hall effect in amorphous CoFeB thin films

Ding Jin-Jun (丁进军), Wu Shao-Bing (吴少兵), Yang Xiao-Fei (杨晓非), Zhu Tao (朱涛)
Chin. Phys. B, 2015, 24 (**2**): 027201. DOI: 10.1088/1674-1056/24/2/027201

On the nature of inhomogeneous weak localization of charge carriers in the heavy fermion compound CeB_6

A N Azarevich[1], A V Bogach[1], O N Khrykina[2], N B Bolotina[2], V M Gridchina[2], S Yu Gavrilkin[3], A Yu Tsvetkov[3], V V Voronov[1], K Flachbart[4], S Gabani[4], and N E Sluchanko[1,†]

[1] *Prokhorov General Physics Institute of the Russian Academy of Sciences, Moscow, Russia*
[2] *Kurchatov Complex of Crystallography and Photonics, National Research Center Kurchatov Institute, Moscow, Russia*
[3] *Lebedev Physical Institute of the Russian Academy of Sciences, Moscow, Russia*
[4] *Institute of Experimental Physics of the Slovak Academy of Sciences, Košice, Slovakia*

(Received 17 May 2025; revised manuscript received 4 July 2025; accepted manuscript online 15 August 2025)

Fine details of the electron density distribution in the heavy fermion metal CeB_6 have been studied for the first time by precision x-ray diffraction experiments in the temperature range of 30–500 K. At temperatures between 30 K and 80 K, the formation of dynamic charge stripes along the $\langle 100 \rangle$ axes is observed in B_6 clusters, corresponding to gapless (weak) localization of charge carriers. Based on the achieved results, we assume that the spin-polarized 5d–2p electronic states in the conduction band are partially localized within these charge stripes and between vibrationally coupled Ce–Ce pairs. Moreover, results of thermal conductivity, heat capacity, Seebeck coefficient and resistivity measurements indicate a significant role of polaron–phonon scattering, which causes inhomogeneous weak localization of charge carriers in CeB_6.

Keywords: weak localization, dynamic charge stripes, heavy fermions

PACS: 72.15.Rn, 72.15.Qm, 71.27.+a

DOI: 10.1088/1674-1056/adfbdd **CSTR:** 32038.14.CPB.adfbdd

1. Introduction

The hexaboride CeB_6 has long been considered as an archetypal example of a magnetic Kondo lattice with a low Kondo temperature $T_K \approx 1$–2 K and two magnetic phase transitions: (i) at $T_Q \approx 3.2$ K to orbital ordering in the so-called antiferroquadrupolar phase (AFQ; "magnetically hidden order" phase) and (ii) at $T_N \approx 2.3$ K into an unusual Néel antiferromagnetic (AFM) ground state.[1–3] However, recent measurements of resistivity and magnetization in the range of $T = 2$–800 K in combination with precise structural studies at temperatures between 85 K and 500 K have shown that CeB_6 is a Griffiths phase with ferromagnetic fluctuations and nanoscale magnetic clusters of Ce ions.[4] Instead of the logarithmic Kondo-type dependence $\sigma(T) \sim \ln T$, which is expected at $T \geq T_K \sim 2$ K, a power-law behavior of conductivity $\sigma(T) \sim T^{0.4}$ is observed in CeB_6 crystals in the range of $T = 8$–80 K $\gg T_K$ (see Fig. 1), corresponding to the regime of weak localization of charge carriers. Indeed, the dependence $\sigma(T) \sim T^{\alpha}$ with $\alpha = 4/11$ was predicted by McMillan for the regime of weak localization in a system with electron–electron interaction in Ref. [5]. Detailed studies of the electron density (ED) distribution using x-ray diffraction (XRD) data at 85 K and in the temperature range of 300–500 K[4,6] led to the conclusion about the formation of (i) vibrationally coupled pairs of Ce ions, (ii) sub-structural charge density waves (s-CDW) with peaks in the interstices of the covalent-bonded B framework and (iii) dynamic charge stripes. At $T_c \approx 340$ K (see Fig. 2), an electronic phase transition associated with a change in the stripe configuration was detected.[6] However, a problem that has not been solved to date is to elucidate the mechanism of weak localization of charge carriers in CeB_6 and the corresponding details of the ED distribution in this heavy fermion metal with nanoscale electron phase separation.

Thus, the goal of present study is to shed more light on the nature of weak localization in the paramagnetic Griffiths phase of CeB_6 with the help of precise XRD experiments in a wide temperature range (30–500 K) in combination with studies of resistivity, Seebeck coefficient, thermal conductivity and heat capacity on high-quality single-domain crystals. Important information on details of the temperature-dependent distribution of electron density in crystals was obtained by the maximum entropy method (MEM) based on detailed XRD data sets collected at fixed temperatures. We suggest that in this heavy fermion metal, electron trapping within vibrationally coupled nanoscale Ce clusters leads to gapless localization in the range of 8–80 K, preceding the transition into the inhomogeneous magnetic AFQ phase with ferromagnetic nanoscale droplets (ferrons)[7] that is observed below $T_Q \approx 3.2$ K. Finally, estimations of the relaxation time and the effective mass of charge carriers are presented, arguing in favor of strong polaron–phonon scattering and renormalization of the electron density of states in CeB_6 at intermediate temperatures.

†Corresponding author. E-mail: nes@lt.gpi.ru

© 2026 Chinese Physical Society and IOP Publishing Ltd. All rights, including for text and data mining, AI training, and similar technologies, are reserved.

2. Experimental details

High-quality CeB_6 single crystals were grown by vertical crucible-free inductive zone melting in an argon gas atmosphere using a setup described in detail in Ref. [8]. For the preparation of CeB_6 we used high-purity substances: natural boron [isotope distribution: 18.8% ^{10}B, 81.2% ^{11}B with purity $>$ 99.9 mass% (AVIABOR Inc., Dzerzhinsk, Russia); the procedure of boron preparation excludes its contamination by carbon] and Ce_2O_3 with purity of 99.997 mass%. The quality and orientation of the samples were controlled by XRD and Laue backscattering patterns. X-ray phase analysis of the synthesized powder and the crushed CeB_6 single crystals was performed on a DRON-3 x-ray diffractometer in Cu $K\alpha$ radiation with a Ni filter and demonstrated only reflections of the CaB_6-type structure (space group $Pm\bar{3}m$-O_h^1). The impurity composition of the grown single crystals was analyzed using an atomic emission spectrometer with inductively coupled plasma iCAP 6500 Duo (Thermo Scientific ICP, USA) with an accepted detection limit of 3 ppm. The presence of oxygen in the grown CeB_6 single crystals was checked using pulsed reductive extraction with carbon in a flow of helium gas (gas chromatography). The oxygen content did not exceed 0.04 mass%, i.e., oxygen is chemically bound to the surface of the crushed single crystal. Thus, the grown CeB_6 crystals and the experimental samples prepared from them represent highly pure and structurally perfect objects for research. The concentration of boron vacancies is estimated to be about 1 at.%.

The sample quality was also characterized by magnetization and charge transport measurements. The single-domain crystals were cut from the same rods as those in Refs. [4,6]. To analyze the transport and thermodynamic properties and scattering mechanisms of charge carriers, the temperature dependences of resistivity (ρ), thermal conductivity (κ) and the Seebeck coefficient (S) were measured in a wide temperature range on rectangular single-crystalline samples 1 mm×2 mm×12 mm in size, elongated in the [110] direction. Heat capacity $C(T)$ was measured on a CeB_6 sample 2 mm× 2 mm×0.5 mm in size. Thermal and transport characteristics were obtained using a commercial installation PPMS-9 (Quantum Design Inc.) of the Shared Research Center of the Lebedev Physical Institute as well as of the Centre of Low Temperature Physics of the Institute of Experimental Physics SAS. Precise XRD experiments on single-crystal samples of CeB_6 were carried out in the temperature range of 30–500 K. XRD data on Ag $K\alpha$ radiation ($\lambda = 0.56087$ Å) were collected on small samples of about 150 μm at the Shared Research Center of the Kurchatov Complex of Crystallography and Photonics of NRC 'Kurchatov Institute' on a Rigaku XtaLAB Synergy-DW diffractometer equipped with a HyPix-Arc 150° photon detector, Cobra Plus and N-Helix cryosystems (Oxford Cryosystems) with open flow of nitrogen and helium gas, respectively. The main experimental results including the structure refinement in the $Pm\bar{3}m$ symmetry group at temperatures of 30 K, 50 K, 70 K, 200 K and 280 K are presented in Table S1 of the supplementary materials. The resistivity and Seebeck coefficient of CeB_6 single crystals were also measured in the temperature range of 300–900 K using an installation of original design.

3. Results and discussion

Temperature dependences of conductivity $\sigma(T) = 1/\rho(T)$ for the direction of measuring current $\boldsymbol{I} \parallel [110]$ and Seebeck coefficient $S(T)$ for the direction of temperature gradient $\nabla T \parallel [110]$ in the temperature range 2–900 K are shown in Fig. 1. The curves obtained for CeB_6 crystals studied in this work are in good agreement with the results of Refs. [2–4,6,9], demonstrating a power-law growth of conductivity $\sigma(T) \sim T^{0.4}$ with increasing temperature in the range of 8–80 K that corresponds to the regime of weak localization of charge carriers predicted in Ref. [5] (see the I_{WL} interval in Fig. 1). Moreover, the logarithmic behavior of the Seebeck coefficient $S(T) \sim -\ln T$, changing from small values $S < 10$ μV·K^{-1}, typical for metals (a degenerate electron gas with $E_F \gg k_B T$, where E_F is the Fermi energy and k_B is the Boltzmann constant), to values $S \sim k_B/e \approx 87$ μV·K^{-1} (e is the charge of an electron), corresponds to a classical electron gas[10] (Fig. 1). The features on the $S(T)$ curves observed at temperatures $T_N \approx 2.4$ K and $T_Q \approx 3.3$ K correspond to transitions to the Néel (III in Fig. 1) and so-called antiferroquadrupole (II) phases of CeB_6, respectively. As shown in earlier work,[2] the Hall coefficient $R_H(T)$ in CeB_6 is negative and almost independent of temperature in the range of 5–300 K. Consequently, the power-law dependence of conductivity is apparently determined exclusively by the behavior of the Hall mobility $\mu_H(T) = R_H(T)\sigma(T)$, which emphasizes the dominant role of scattering processes in the charge transport of CeB_6 in the temperature range of 8–80 K. Figure 1 also shows the additive parameter $\sigma(T)S(T)$ whose behavior indicates the absence of other contributions at temperatures corresponding to weak localization of charge carriers in the interval I_{WL}.

The separation of additive contributions to $\sigma(T)S(T)$ allows us to identify and analyze the high-temperature component of the Seebeck coefficient in CeB_6 with a maximum in the region of $T_{max}^S \sim 200\ K \ll \theta_D \sim 1100$ K,[11] where θ_D is the Debye temperature, which corresponds to the contribution of phonon drag effects. In accordance with predictions made in Ref. [10], a dependence $S_L(T) \sim 1/T$ is observed on the right side of the maximum of lattice thermopower, while the low-temperature phonon drag dependence demonstrates a quadratic asymptotic behavior $S_L(T) \sim T^2$ (see Fig. 1), which apparently indicates a decrease of the effective dimensional-

ity of the charge transport in the interval $T < \theta_E \sim 130$ K,[11] where θ_E is the Einstein temperature.

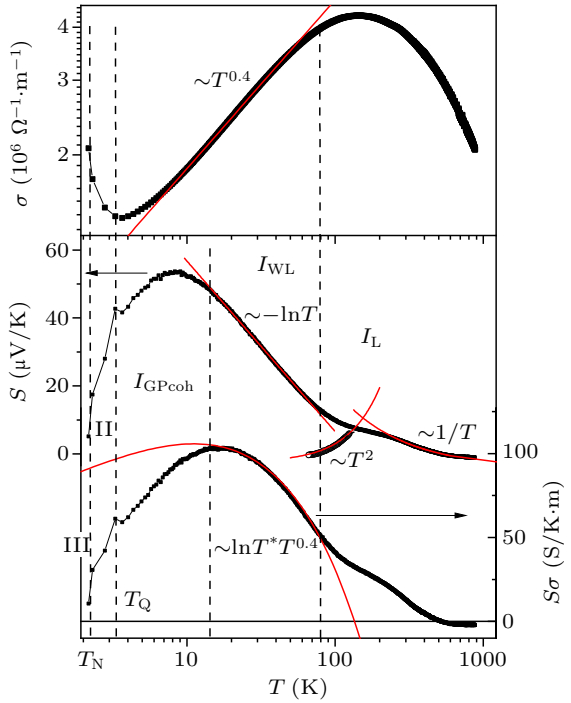


Fig. 1. Temperature dependences of conductivity $\sigma(T)$, the Seebeck coefficient $S(T)$ and the additive parameter $\sigma(T)S(T)$. Vertical dashed lines separate the temperature intervals corresponding to the phonon drag (I_L interval), weak localization (I_{WL}), coherent Griffiths phase (I_{GPcoh})[7] regimes of charge carrier transport and the magnetically ordered phases (II and III) of CeB_6.

Figure 2 shows the results of structural studies of single-crystal samples of CeB_6 in the temperature range of 30–500 K. The temperature dependences of lattice periods and angles demonstrate small static Jahn–Teller (JT) distortions of the cubic lattice upon cooling below room temperature, which noticeably increase below 80 K in the range I_{WL} of weak localization of charge carriers. The linear and angular static distortions of the cubic lattice do not exceed 0.003 Å and 0.1°, respectively, which does not require a transition to a non-cubic structural model.

ED distribution maps in three families of {110} planes (Fig. 3) were obtained by the MEM (see supplementary materials for more details) using XRD data collected at temperatures of 30 K, 50 K, 70 K, 200 K and 280 K. The ED peaks in Fig. 3 are cut at the 2 electrons/voxel level to show fine details of ED distribution between atomic positions. Although {110} planes should be equivalent in the $Pm\bar{3}m$ symmetry group, the differences in the ED distribution appear due to small static JT distortions of the crystal lattice (Fig. 2), which are accompanied by the cooperative dynamic JT instability of the crystal structure.[4,6] In most {110} planes, strong ED distortions (non-round, smeared EDs) are observed near the Ce^{3+} ions, indicating the formation of vibrationally coupled magnetic clusters of Ce (examples are shown by ellipses in Fig. 3, arrows indicate the direction of Ce–Ce vibrations). Additionally, with stripes in some {110} planes at intermediate temperatures of 100–500 K, we observed sub-structural charge density wave peaks (see, for example, the s-CDW marked with small yellow circles in Fig. 3 at $T = 200$ K in the (1-10) plane), previously discovered both in CeB_6 above room temperature[6] and in ZrB_{12} in a wide temperature range.[12] In the range 30–80 K of weak localization of charge carriers (I_{WL}), dynamic charge stripes of ED are formed predominantly in the 2p states on boron atoms, which are clearly visible in the (01-1) and (1-10) planes (indicated by vertical lines in Fig. 3). Analysis of the ED distribution In the (01-1) plane (left column) at $T = 30$ K shows that due to quasi-local vibrations of Ce ions in ⟨111⟩ directions, the 5d orbitals, which are hybridized with 4f states of Ce (spin-polarons[2]), are mixed with the linear dynamic charge stripe formed by 2p electrons of B atoms. It can be assumed that the described mutual arrangement of B 2p states in stripe and spin polarized 5d (4f) conduction electrons determines the mechanism of weak localization of charge carriers in this metal with heavy fermions.

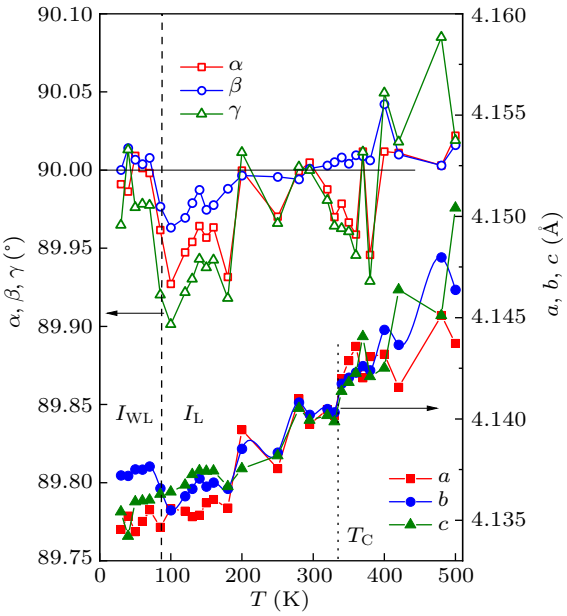


Fig. 2. Temperature dependences of periods and angles in the lattice of CeB_6.

It should be emphasized that the ED distribution presented in Fig. 3 is not in accordance with the generally accepted Kondo lattice scenario based on only one quantum mechanical instability of the 4f shell of the Ce^{3+} ions, which produces 4f–5d spin fluctuations around the Ce ions. The results obtained in the range far above the Kondo temperature $T_K \sim 2$ K demonstrate that most charge fluctuations are a natural consequence of the JT cooperative instability of B_6 clusters, which causes transverse quasi-local vibrations of magnetic Ce ions. It can be assumed that it represents a combination of the JT structural instability of the boron framework with the 4f–5d spin fluctuations on Ce sites that leads to the spin-polaron effect,[2,7,13,14] resulting in the localization of ED

near the charge stripes and between vibrationally bound Ce–Ce pairs.

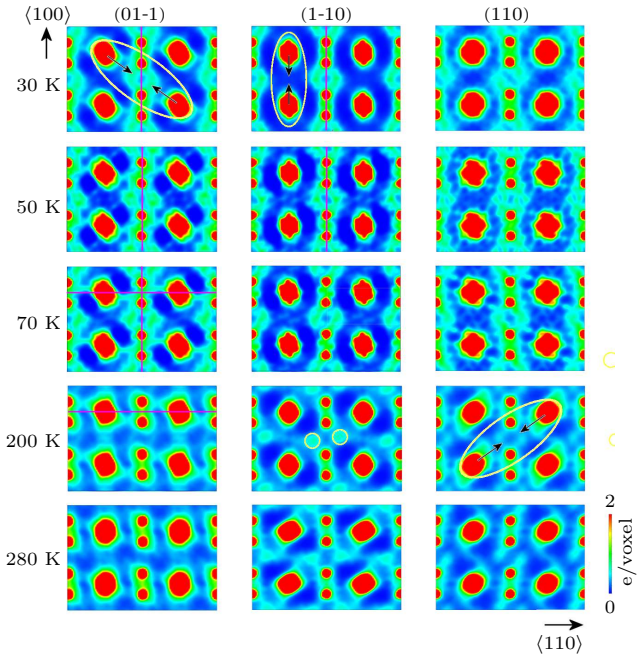


Fig. 3. Maps of the electron density distribution in CeB_6 obtained by the MEM at temperatures of 30 K, 50 K, 70 K, 200 K and 280 K (from top to bottom) in (from left to right) (01-1), (1-10) and (110) planes. The calculations were performed without constraints on the $Pm\bar{3}m$ symmetry. The planes pass through Ce atoms (large red spots) and two of the six B atoms (small red spots) forming the octahedron B_6. The ED peaks are cut at the 2 electrons/voxel level. Directions along which the charge stripes are most likely to form are indicated by straight lines. Arrows within the ellipses show the direction of ED displacements leading to the formation of Ce–Ce pairs. Small yellow circles in the (1-10) plane (middle column) at 200 K mark the s-CDW peaks in CeB_6 (see text for more details).

Similar nanoscale heterogeneity (stripes) has also been observed in magnetic GdB_6[15] and in non-magnetic reference hexaboride LaB_6,[4,16] in which record thermionic emission was found, and is widely used in numerous practical applications.[17] Studies of wideband dynamic conductivity of LaB_6 single crystals with various ^{10}B and ^{11}B isotope contents[18] and of $Gd_xLa_{1-x}B_6$ substitutional solid solutions[19] allow the conclusion that only a small fraction of conduction electrons behave as Drude-type charge carriers, while about 70% of electrons are involved in collective oscillations of the electron density coupled to vibrations of both the JT unstable rigid boron cage and the rattling modes of heavy La (Gd) ions loosely bound to the lattice. It has been suggested[18] that the non-equilibrium (hot) conduction electrons determine the extraordinarily low work function of thermionic emission in LaB_6. Besides, the collective JT mode (ferrodistortive effect; see, for example, Ref. [20] for more detail) is the trigger responsible in rare earth high borides for the periodic changes in hybridization of the 5d–2p conduction band states, leading to the nanoscale electron phase separation (dynamic charge stripes). We assume that both B vacancies and ^{10}B–^{11}B substitutional disorder should be regarded as effective stripe pinning centers in CeB_6, and this issue is planned to be investigated in the future.

The boron JT cooperative dynamics induces quasilocal vibrations ($\hbar\omega_E \sim 12$ meV,[21,22] ω_E being the Einstein frequency) of Ce ions in Ce–Ce pairs along the ⟨110⟩ and ⟨111⟩ directions (Fig. 3 and Ref. [7]). The contribution of 5d states of Ce to the predominantly 2p-type stripes of B chains is detected clearly in Fig. 3 (for example, in the plane (01-1) at $T = 30$ K). These many-body states are spin-polarized because of fast local 4f–5d spin fluctuations,[2] and we suggest that these Einstein-type vibrations of Ce ions in Ce–Ce pairs in the directions intersecting stripes are responsible for the enhancement of the electron density of states (DOS) $N(E_F)$, leading to formation of heavy fermions with low mobility values.[2] DOS increases under coolling (appearance and enhancement of the many-body resonance in CeB_6; see the estimation of the effective mass of charge carriers below) in the weak localization temperature range of 8–80 K (I_{WC}), and the occurrence of ferrons below T_Q[7] can be explained in terms of the Stoner-type ferromagnetic instability criterion $UN(E_F) \geq 1$ (where U is the Coulomb repulsion energy).[2] It should be noted that CeB_6 differs greatly from other rare earth hexaborides due to intense ferromagnetic (FM) fluctuations that are a feature of the Griffiths phase regime. Indeed, a low-energy collective FM mode in the magnetic excitation spectrum of CeB_6 was found in inelastic neutron scattering experiments.[23] The results of electron spin resonance,[24,25] muon spin relaxation (μSR) spectroscopy,[26,27] Hall effect,[2] magnetoresistance, thermal conductivity and heat capacity studies[7] of CeB_6 confirmed the appearance of ferromagnetic nano-domains embedded in the CeB_6 matrix, which places CeB_6 much closer to FM instability than previously thought. Thus, we suggest that 4f–5d–2p charge and spin fluctuations near the dynamic charge stripes are responsible for the DOS renormalization effect in CeB_6, and that the role of spin polarization of 5d states is important. In particular, in the nonmagnetic reference compound LaB_6 a mechanism of localized inhomogeneous superconductivity induced by Cooper pairing mediated by quasilocal vibrations of La ions was proposed very recently,[16] but the weak localization effect was not observed in this case.

To shed more light on the polaron–phonon mechanism of weak localization of charge carriers in CeB_6, thermal conductivity and heat capacity data analysis was performed (Fig. 4(a)) and the behavior of relaxation time and effective mass of charge carriers was estimated (Fig. 4(b)). The dependences of $\kappa(T)$ and $C(T)$ (Fig. 4(a)) are in good agreement with the results in Ref. [30]. Under cooling to $T_s \sim 15$ K, the heat capacity deviates from the exponential Einstein-type asymptotic ($\theta_E \sim 130$ K[11]) with the power-law dependence $C(T) \sim T^{-0.8}$, indicating a transition to Griffiths phase behavior, which is reliably demonstrated in the wide interval 5–

800 K on magnetization curves of CeB_6.[4] In this temperature range (I_{GPcoh} in Fig. 4), a power-law dependence of thermal conductivity in the form $\kappa(T) \sim T^{2.2}$ is observed, which apparently indicates an electron–phonon scattering mechanism. Using the relation for thermal conductivity based on the electron gas approximation in the range of 5–15 K (I_{GPcoh} in Fig. 4)

$$\kappa(T) = \frac{1}{3} C(T) \cdot v_F^2 \cdot \tau(T), \tag{1}$$

where $v_F \approx 1.1 \times 10^6$ cm·s^{-1} is the Fermi velocity found from measurements of quantum oscillations in CeB_6 by the magneto-acoustic method;[31] we obtain a $\tau(T) \sim T^3$ power-law dependence for the charge carrier relaxation time (Fig. 4(b)). For comparison, Fig. 4(b) shows the relaxation time curves obtained by μSR spectroscopy[28] and quasi-elastic neutron scattering,[29] as well as the values of τ_{ferr} and τ_0 components deduced in Ref. [7] at $T_0 = 1.9$ K by the analysis of magnetic field dependences of heat capacity and thermal conductivity using the separation of contributions in the magnetically ordered phase II of CeB_6. According to the conclusions in Ref. [7], the values of $\tau_{ferr} \approx 1.3 \times 10^{-14}$ s and $\tau_0 \approx 3.3 \times 10^{-12}$ s (Fig. 4(b)) are characteristic of charge carrier scattering on spin droplets (ferrons) and on dynamic charge stripes, respectively. The value of $\tau_0(T_0)$ is comparable to $\tau(T_s = 15\ \text{K}) \approx 3.9 \times 10^{-12}$ s obtained from the analysis within the framework of Eq. (1), corresponding to the vibration frequency (∼ 240 GHz) of the electron density in 5d–2p dynamic charge stripes, which was found from optical spectra measurements in higher borides $Tm_{1-x}Yb_xB_{12}$.[32] Besides, $\tau_{ferr}(T_0 = 1.9\ \text{K})$ is in accord with the extrapolation $\tau(T) \sim T^3$ of the experimental curve in the low-temperature interval (see Fig. 4(b)). In this regard, it should be assumed that at $T_s \sim 15$ K a crossover is observed from predominant carrier scattering on dynamic charge stripes to scattering on ferromagnetic fluctuations in the Griffiths phase of CeB_6. The dramatic DOS renormalization effect in the range of 15–400 K (about 15 times increase of the effective mass) was estimated here in the framework of the simple Drude formula $m^*(T)/m_0 = e\tau(T)/(\mu_H(T)m_0)$ (see Fig. 4(b); m_0 is the free electron mass). We suggest that in the range of 5–15 K (see I_{GPcoh} in Fig. 4) local regions of spin polarization are formed in the neighborhood of dynamic charge stripes, and both the effective mass and the relaxation time decrease strongly (Fig. 4(b)). These many-body states are transformed into spin droplets (ferrons) during the transition to magnetically ordered phase II. We suggest that the approximation of the relaxation time by $\tau(T) \sim T^3$ dependence (see Fig. 4(b)) found in this work characterizes the process of the direct creation from heavy fermions of the spin-polarized many-body states inside and between B_6 clusters. It should be also noted that the electron spin density distribution of CeB_6, found in Ref. [33] by the MEM using polarized neutron diffraction data analysis at $T = 1.6$ K, revealed the presence in phase II of magnetic moments of about 0.3 μ_B, localized both between B_6 clusters and in the centers of triangular faces of B_6 octahedra. The latter result is also consistent with the spin-polaron 5d component of the magnetic structure found in Refs. [2,7,13,14] with spin density peaks located in the interstitial sites of the CeB_6 cubic lattice.

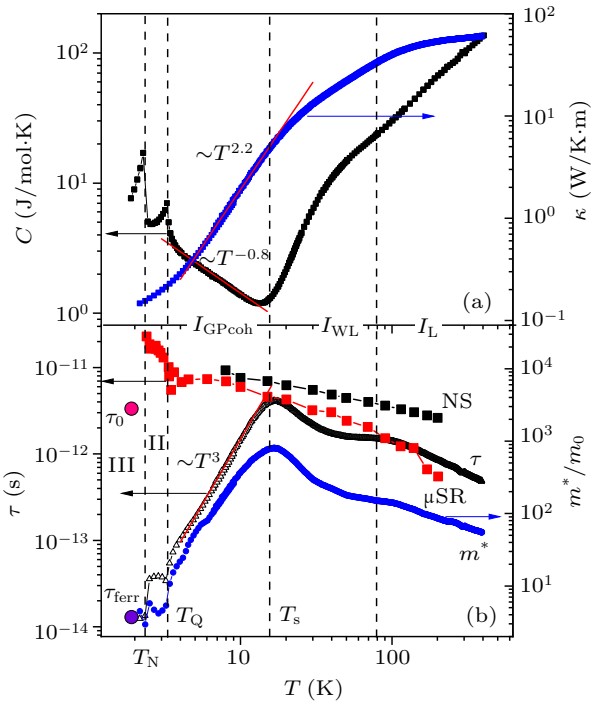


Fig. 4. Temperature dependences of (a) specific heat and thermal conductivity and (b) the relaxation time (see Eq. (1)) and effective mass of charge carriers in CeB_6. Red straight lines show the approximation of $C(T)$, $\kappa(T)$ and $\tau(T)$ experimental curves by power-law dependences in the interval 5–15 K (I_{GPcoh}), corresponding to the coherent Griffiths phase. Panel (b) shows the relaxation curves obtained from μSR spectroscopy[28] and from quasi-elastic neutron scattering (NS)[29] measurements. The values of τ_{ferr} and τ_0 were obtained in Ref. [7] at $T = 1.9$ K for the magnetically ordered AFQ phase (II) of CeB_6 from the analyses of magnetic field dependences of heat capacity and thermal conductivity using the separation of contributions from carrier scattering on ferrons and dynamic charge stripes, respectively.

4. Conclusions

Precise XRD experiments in the temperature range of 30–500 K revealed small static JT structural distortions in combination with the formation of (i) dynamic charge stripes along some of ⟨100⟩ and ⟨110⟩ directions of the cubic lattice of CeB_6, (ii) vibrationally coupled nanoscale clusters of Ce ions and (iii) the appearance of sub-structural charge density waves. The analysis of the obtained ED distribution performed by the MEM leads to the conclusion that in the temperature range of 30–80 K the dynamic charge stripes are predominantly arranged on the 2p states of B_6 clusters. This analysis also allowed us to suggest a mechanism for weak localization of charge carriers. Its essence is that the electron density in the 5d–2p conduction band is partially spin-polarized because of

fast 4f–5d spin fluctuations on Ce sites and localized weakly between vibrationally coupled Ce nanoscale clusters in the close vicinity of dynamic charge stripes. Based on the results of thermal conductivity, heat capacity, Seebeck coefficient and resistivity measurements, variations of both the relaxation time and the effective mass of charge carrier were estimated. We argue that the weak localization phenomenon is accompanied by the strong renormalization of the electron density of states $N(E_F)$ and effective mass enhancement, reaching the Stoner criterion for ferromagnetism at liquid helium temperatures. This points to a crossover from charge carrier scattering on dynamic charge stripes (with $\tau_0 \approx 3.3 \times 10^{-12}$ s, frequency $\sim$ 300 GHz) to scattering on ferromagnetic fluctuations below $T_s \sim 15$ K in the coherent Griffiths phase regime, which is accompanied by the relaxation time behavior $\tau(T) \sim T^3$ and leads to the formation of spin-polarized nanodomains (ferrons) observed recently[7] in the CeB_6 matrix.

Acknowledgements

S.G. and K.F. acknowledge the support of the Slovak Research and Development Agency under contract No. APVV-23-0226 and VEGA 2/0034/24. The work was partly performed using the equipment of the Shared Research Centers of the Kurchatov Complex of 'Crystallography and Photonics' of NRC Kurchatov Institute and Lebedev Physical Institute of RAS. The work of O.N. Khrykina, N.B. Bolotina and V.M. Gridchina in the part of structural analysis was performed within the framework of the State Assignment of NRC 'Kurchatov Institute'. The authors are grateful to S.V. Demishev and V.V. Glushkov for useful discussions.

References

[1] Zirngiebl E, Hillebrands B, Blumenröder S, Güntherodt G, Loewenhaupt M, Carpenter J M, Winzer K and Fisk Z 1984 *Phys. Rev. B* **30** 4052
[2] Sluchanko N E, Bogach A V, Glushkov V V, Demishev S V, Ivanov V Y, Ignatov M I, Kuznetsov A V, Samarin N A, Semeno A V and Shitsevalova N Y 2007 *J. Exp. Theor. Phys.* **104** 120
[3] Cameron A S, Friemel G and Inosov D S 2016 *Rep. Prog. Phys.* **79** 66502
[4] Khrykina O N, Bolotina N B, Gridchina V M, Azarevich A N, Bogach A V, Demishev S V, Krasikov K M, Shitsevalova N Yu, Filipov V B, and Sluchanko N E 2024 *J. Alloys Compd.* **970** 172527
[5] McMillan W L 1981 *Phys. Rev. B* **24** 2739
[6] Khrykina O N, Bolotina N B, Gridchina V M, Azarevich A N, Krasikov K M, Shitsevalova N Yu, Filipov V B, Gavrilkin S Yu, Tsvetkov A Yu and Sluchanko N E 2024 *JETP Lett.* **119** 144
[7] Azarevich A N, Khrykina O N, Bolotina N B, Gridchina V G, Bogach A V, Demishev S V, Krasnorussky V N, Gavrilkin S Yu, Tsvetkov A Yu, Shitsevalova N Yu, Voronov V V, Kugel K I, Rakhmanov A L, Gabáni S, Flachbart K and Sluchanko N E 2025 *Solid St. Sci.* **167** 107990
[8] Shitsevalova N 2021 *Rare-Earth Borides* (Ed. by Inosov D S) (Singapore: Jenny Stanford Publishing) pp. 1–244
[9] Ignatov M I, Bogach A V, Glushkov V V, Demishev S V, Paderno Yu B, Shitsevalova N Yu and Sluchanko N E 2006 *Physica B* **378–380** 780
[10] Chaikin P M 1990 *Organic Superconductivity* (Ed. by Kresin V Z and Little W A) (New York: Plenum Press) p. 101
[11] Kunii S, Effantin J M and Rossat-Mingnod J 1997 *J. Phys. Soc. Jpn.* **66** 1029
[12] Bolotina N B, Khrykina O N, Azarevich A N, Shitsevalova N Y, Filipov V B, Gavrilkin S Y, Tsvetkov A Y, Gabáni S, Flachbart K, Voronov V V and Sluchanko N E 2023 *Solid State Sci.* **142** 107245
[13] Sluchanko N E, Anisimov M A, Bogach A V, Voronov V V, Glushkov V V, Demishev S V, Krasnorusskii V N, Gavrilkin S Y, Filippov V B and Shitsevalova N Y 2015 *JETP Lett.* **101** 36
[14] Sluchanko N E, Bogach A V, Glushkov V V, Demishev S V, Ivanov V Y, Shitsevalova N Y and Filipov V B 2008 *JETP Lett.* **88** 318
[15] Dudka A P, Khrykina O N, Bolotina N B, Shitsevalova N Yu, Filipov V B, Anisimov M A, Gábani S, Flachbart K and Sluchanko N E 2019 *Phys. Rev. B* **100** 205103
[16] Azarevich A N, Bogach A V, Khrykina O N, Bolotina N B, Gridchina V M, Shitsevalova N Yu, Gavrilkin S Yu, Tsvetkov A Yu, Gabáni S, Flachbart K, Kuznetsov A V, Sluchanko N E 2024 *JETP Lett.* **119** 934
[17] Trenary M 2012 *Sci. Technol. Adv. Mater.* **13** 023002
[18] Zhukova E S, Gorshunov B P, Dressel M, Komandin G A, Belyanchikov M A, Bedran Z V, Muratov A V, Aleshchenko Y A, Anisimov M A, Shitsevalova N Yu, Dukhnenko A V, Filipov V B, Voronov V V and Sluchanko N E 2019 *JETP Lett.* **110** 79
[19] Zhukova E S, Gorshunov B P, Komandin G A, Alyabyeva L N, Muratov A V, Aleshchenko Yu A, Anisimov M A, Shitsevalova N Yu, Polovets S E, Filipov V B, Voronov V V and Sluchanko N E 2019 *Phys. Rev. B* **100** 104302
[20] Bolotina N B, Dudka A P, Khrykina O N and Mironov V S 2021 *Rare-Earth Borides* (Ed. by Inosov D S) (Singapore: Jenny Stanford Publishing) pp. 293–330
[21] Smith H G, Dolling G, Kunii S, Kasaya M, Liu B, Takegahara K, Kasuya T and Goto T 1985 *Solid State Commun.* **53** 15
[22] Kunii S, Effantin J M and Rossat-Mingnod J 1997 *J. Phys. Soc. Jpn.* **66** 1029
[23] Jang H, Friemel G, Ollivier J, Dukhnenko A V, Shitsevalova N Y, Filipov V B, Keimer B and Inosov D S 2014 *Nat. Mater.* **13** 682
[24] Demishev S V, Semeno A V, Bogach A V, Samarin N A, Ishchenko T V, Filipov V B, Shitsevalova N Yu and Sluchanko N E 2009 *Phys. Rev. B* **80** 245106
[25] Semeno A V, Gilmanov M I, Bogach A V, Krasnorussky V N, Samarin A N, Samarin N A, Sluchanko N E, Shitsevalova N Yu, Filipov V B, Glushkov V V and Demishev S V 2016 *Sci. Rep.* **6** 39196
[26] Schenck A, Gygax F N and Kunii S 2002 *Phys. Rev. Lett.* **89** 037201
[27] Schenck A, Gygax F N, Solt G, Zaharko O and Kunii S 2004 *Phys. Rev. Lett.* **93** 257601
[28] Gygax F N, Schenck A, Solt G and Zaharko O 2010 *Phys. Rev. B* **81** 094434
[29] Horn S, Steglich F, Loewenhaupt M, Scheuer H, Felsch W and Winzer K 1981 *Z. Phys. B: Condens. Matter* **42** 125
[30] Peysson Y, Ayache C, Salce B, Rossat-Mignod J, Kunii S and Kasuya T 1985 *J. Magn. Magn. Mater.* **47–48** 63
[31] Goto T, Suzuki T, Ohe Y, Fujimura T and Tamaki A 1988 *J. Magn. Magn. Mater.* **76–77** 305
[32] Zhukova E, Melentyev A, Gorshunov B, Muratov A, Aleshchenko Yu, Azarevich A, Krasikov K, Shitsevalova N, Filipov V and Sluchanko N 2022 *J. Phys.: Condens. Matter* **34** 465603
[33] Saitoh M, Okada N, Nishibori E, Takagiwa H, Yokoo T, Nishi M, Kakurai K, Kunii S, Takata M, Sakata M and Akimitsu J 2002 *J. Phys. Soc. Jpn.* **71** 2369